Demonstration of 1 Million Q-Factor on Microglassblown Wineglass Resonators With Out-of-Plane Electrostatic Transduction

Doruk Senkal, *Student Member, IEEE*, Mohammed J. Ahamed, *Member, IEEE*, Mohammad H. Asadian Ardakani, *Student Member, IEEE*, Sina Askari, *Student Member, IEEE*, and Andrei M. Shkel, *Fellow, IEEE*

***Abstract*— In this paper, we report Q-factor over 1 million on both $n = 2$ wineglass modes, and high-frequency symmetry ($\Delta f/f$) of 132 ppm on wafer-level microglassblown 3-D fused silica wineglass resonators at a compact size of 7-mm diameter and center frequency of 105 kHz. In addition, we demonstrate for the first time, out-of-plane capacitive transduction on micro-electromechanical systems wineglass resonators. High Q-factor is enabled by a high aspect ratio, self-aligned glassblown stem structure, careful surface treatment of the perimeter area, and low internal loss fused silica material. Electrostatic transduction is enabled by detecting the spatial deformation of the 3-D wineglass structure using a new out-of-plane electrode architecture. Out-of-plane electrode architecture enables the use of sacrificial layers to define the capacitive gaps and 10 μm capacitive gaps have been demonstrated on a 7-mm shell, resulting in over 9 pF of active capacitance within the device. Microglassblowing may enable batch-fabrication of high-performance fused silica wineglass gyroscopes at a significantly lower cost than their precision-machined macroscale counterparts. [2014-0251]**

***Index Terms*— Micro-glassblowing, 3-D MEMS, wineglass resonator, degenerate mode gyroscope, fused silica.**

I. Introduction

CORIOLIS vibratory gyroscopes (CVGs) can be divided into two broad categories based on the gyroscope 's mechanical element [1]: degenerate mode gyroscopes which have x-y symmetry (Δf of 0 Hz for a z-axis gyro) and non-degenerate mode gyroscopes which are designed intentionally to be asymmetric in x and y modes (Δf of 10 to 100 Hz for a z-axis gyro). Despite potential advantages of degenerate mode operation (high rate sensitivity and whole-angle operation), historically, most high-performance MEMS CVGs have been designed to operate as non-degenerate mode devices, whereas degenerate mode operation was reserved for precision machined macro-scale CVGs, such as the Hemi-spherical Resonator Gyroscope (HRG) [2]. This is mainly due to the high structural symmetry, or equivalently high frequency symmetry (Δf) required for degenerate mode operation, making large-scale fabrication of these devices challenging due to large relative tolerances and low aspect ratios associated with conventional micro-machining processes. Factors such as mold non-uniformity, high surface roughness and granularity of deposited thin films have so far prevented the integration of 3-D wineglass structures with MEMS techniques.

Primarily, two main methods are employed in fabrication of MEMS wineglass structures: (1) deposition of thin-films on pre-defined molds, (2) blow molding the device layer into a pre-defined cavities. For example, Q-factor of 19.1k have been demonstrated on poly-silicon shell structures deposited in pre-etched cavities [3]. Q-factors up to 24k [4] were measured on poly-diamond wineglass shells deposited in pre-etched cavities and up to 20k were measured on sputtered Ultra Low Expansion (ULE) glass shells deposited on precision ball lenses [5]. Q-factors as high as 7.8k was demonstrated on blow-molded bulk metallic glass shells [6] and 1 million on fused silica shells [7].

Aside from challenges associated with obtaining a high-Q resonator with low frequency split (Δf), defining electrodes on these 3-D MEMS structures with sufficiently small gaps and uniformity provides an additional challenge for gyroscope operation. For thin film devices this is accomplished by defining electrode structures within the pre-etched cavity by placing a sacrificial layer in between the electrode and the device [4], [8]. For glassblown devices a wide variety architectures have been demonstrated, including deep glass dry etching of the capacitive gaps [9] ($>30\mu$m), utilization of thermal mismatch between the shell and the mold to create the capacitive gaps [6] ($\sim 15\mu$m), and various assembly techniques [10], [11] ($\sim 15\mu$m). Despite these advances, factors such as alignment errors between the shell and the electrodes, cross-talk between electrodes, relatively large gaps created by assembly based techniques and lack of scalability remain a challenge.

In this paper, we explore an alternative fabrication paradigm under the hypothesis that surface tension and pressure driven micro-glassblowing process may serve as an enabling mechanism for wafer-scale fabrication of extremely symmetric and atomically smooth wineglass resonators [12].

Manuscript received August 19, 2014; revised September 30, 2014; accepted October 17, 2014. Date of publication November 13, 2014; date of current version January 30, 2015. This work was supported by the Defense Advanced Research Projects Agency, Arlington, VA, USA, under Grant W31P4Q-11-1-0006. (Program Manager Dr. Robert Lutwak.) Subject Editor R. T. Howe.

The authors are with the University of California at Irvine, Irvine, CA 92697 USA (e-mail: dsenkal@uci.edu; mahamed@uci.edu; asadianm@uci.edu; askaris@uci.edu; ashkel@uci.edu).

Color versions of one or more of the figures in this paper are available online at http://ieeexplore.ieee.org.

Digital Object Identifier 10.1109/JMEMS.2014.2365113

Micro-glassblowing process relies on viscous deformation of the device layer under the influence of surface tension and pressure forces to define the 3-D shell structure as opposed to conventional deposition, molding, or etching techniques. During the brief duration, while the device layer is still viscous, surface tension forces act on the 3-D shell structure, at an atomic level, to minimize surface roughness and structural imperfections; this leads to levels of smoothness and structural symmetry that is not available through conventional fabrication techniques. In addition, current MEMS fabrication techniques restrict the material choice to a few materials limiting the maximum achievable Q-factor. Available materials, such as single-crystal silicon, have relatively high Coefficient of Thermal Expansion (CTE on the order of 3 ppm/°C [13]) and consequently high Thermoelastic Dissipation (TED). Materials with low CTE, such as fused silica (0.5 ppm/°C) or Ultra Low Expansion Titania Silicate Glass (ULE TSG, 0.03 ppm/°C), provide a dramatic increase in fundamental Q_{TED} limit. ULE TSG is a glass that consists of SiO_2 and TiO_2; this engineered material has the lowest known isotropic CTE. However, when compared to silicon, titania silicate glass and fused silica dry etching suffers from an order of magnitude higher surface roughness, lower mask selectivity (1:1 for KMPR photoresist), and lower aspect ratio, <6:1 [14]. Micro-glassblowing allows the use of fused silica material on a wafer-level without the need for these challenging dry etching techniques. Despite these potential advantages, the 3-D micro-glassblowing paradigm brings forth challenges for electrode integration, due to the high aspect ratio, aspherical resonator element, and high temperature fabrication process (1700 °C). To address these challenges we propose an out-of-plane electrode architecture. Transduction is enabled by detecting and driving the spatial modes of the 3-D wineglass resonator, which allows one to drive and sense the wineglass modes using their out-of-plane components.

Micro-glassblowing of borosilicate glass spherical shell structures have been demonstrated for nuclear magnetic resonance applications [15]. Later, fused silica and ultra low expansion glass micro-glassblowing of inverted-wineglass structures have been demonstrated at temperatures as high as 1700 °C [12]. Assembled electrode structures [11], as well as deep glass dry etched electrode structures have been developed for electrostatic transduction of micro-glassblown structures [9], [14]. Finite element analysis of the micro-glassblowing process [16], and further improvement in the fabrication process led to frequency splits between the wineglass modes (Δf) as low as 0.16 Hz on borosilicate glass wineglass structures [9].

In this work, we report the most recent developments in the wafer-level, micro-glassblowing paradigm for fabrication of 1 million Q-factor, highly symmetric ($\Delta f/f = 132$ ppm) fused silica wineglass resonators at 7 mm diameter, Fig 1. And we demonstrate out-of-plane electrostatic transduction on MEMS wineglass resonators with uniform 10 μm capacitive gaps resulting in over 9 pF of active capacitance within the device.

In the following sections, we will first present design of out-of-plane architecture and discuss parameters affecting Q-factor, Section II. This will be followed by analytical and finite element models for predicting the final geometry of the micro-glassblown structure, Section III. In Section IV, we will present the fabrication process for fused silica wineglass resonators with out-of-plane electrodes. In Section V, we will present frequency and time domain characterization of wineglass resonators. The paper concludes with a discussion of the results, Section VI.

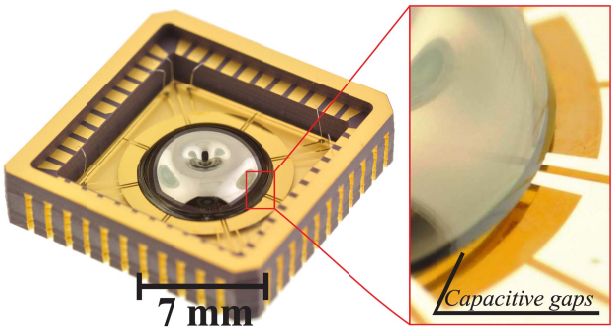

Fig. 1. 1 million Q-factor fused silica wineglass structure with integrated electrodes (left), close-up of capacitive gaps (right).

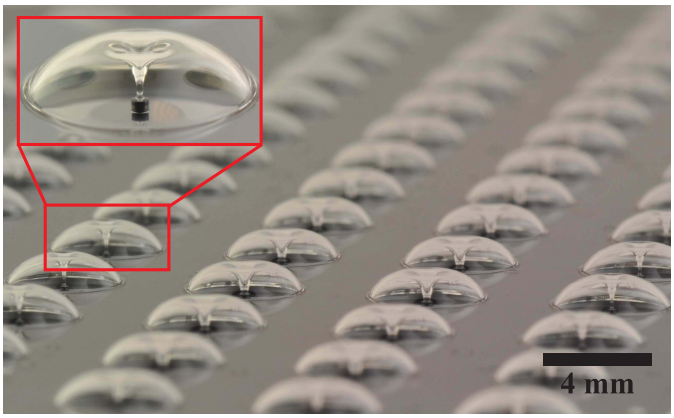

Fig. 2. Micro-glassblowing process can create arrays of inverted-wineglass structures on the wafer surface. Outer diameter of shells is ~4 mm, over 100 shells were fabricated on a 4" wafer.

II. Design

Out-of-plane electrode architecture and parameters affecting Q-factor are discussed in this section.

A. Out-of-Plane Electrode Architecture

Wineglass Coriolis Vibratory Gyroscopes (CVGs) typically utilize 8 or more electrodes to drive and sense the primary wineglass modes. One of the main challenges of fabricating micro-wineglass resonators is the definition of electrode structures in a manner compatible with batch-fabrication, Fig. 2. 3-D side-walls of the wineglass geometry makes it challenging to fabricate radial electrodes with small capacitive gaps and to keep the gap uniform across the height of the structure. Even though post-fabrication assembly techniques have been successfully demonstrated [10], [11], these approaches create a bottle-neck in batch-fabrication of the devices at wafer level.

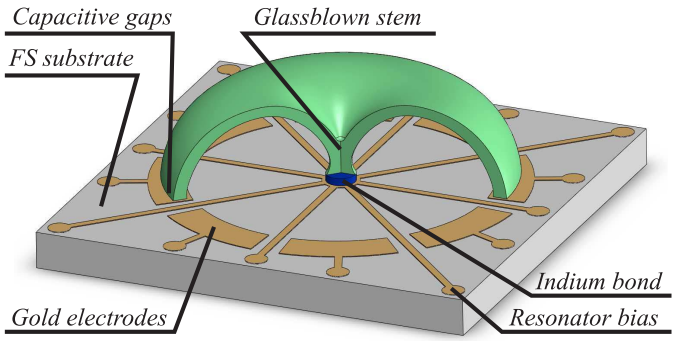

Fig. 3. Out-of-plane electrode architecture consists of a micro-glassblown fused silica (FS) wineglass resonator and planar Cr/Au electrodes defined on fused silica, enabling batch-fabrication.

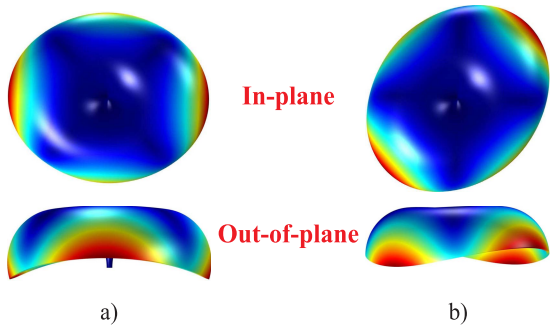

Fig. 4. Out-of-plane transduction scheme utilizes out-of-plane component of wineglass modes to drive and sense in-plane motion. (a) 1st n = 2 wineglass mode. (b) 2nd n = 2 wineglass mode.

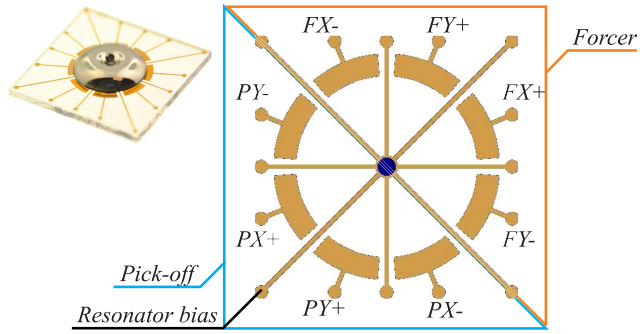

Fig. 5. Electrode configuration used in this paper. 4 electrodes are designated as forcer (FX and FY) and 4 are designated as pick-off (PX and PY). Both the forcer and pick-off channels have differential pairs (i.e. FX+ and FX−).

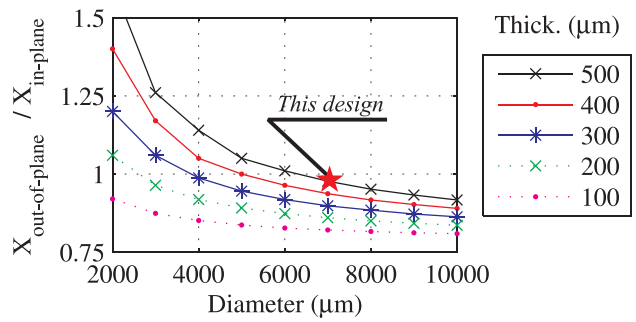

Fig. 6. Out-of-plane to in-plane displacement ratio for mushroom resonators: Due to the 3-D nature of the resonator, the ratio is close to 1:1. Star marks the design presented in this paper.

In this paper, we explore an alternative transduction paradigm based on out-of-plane electrode architecture. The architecture consists of a micro-glassblown fused silica wineglass resonator and planar Cr/Au electrodes defined on a fused silica substrate, Fig. 3. Out-of-plane capacitive gaps are formed between the Cr/Au metal traces and the perimeter of the wineglass resonator. Electrostatic transduction is made possible by the 3-D mode shape of the wineglass resonator. In-plane deformation of wineglass modes is accompanied by an out-of-plane deformation, Fig. 4. This permits the use of out-of-plane transduction to drive and sense the in-plane oscillations, which are sensitive to coriolis forces along the z-axis of the structure [17].

In our implementation, a total of 8 electrodes are used, which is the minimal configuration to drive and sense the n = 2 wineglass modes. 4 electrodes are designated as forcer (FX and FY) and 4 are designated as pick-off (PX and PY). Both the forcer and pick-off channels have differential pairs (i.e. FX+ and FX−). The resonator is biased using any of the 8 traces that extend from the central anchor point. These traces also help suppress parasitic coupling between adjacent electrodes by sinking stray currents, Fig. 5.

As the thickness of the shell limits the maximum surface area for the out-of-plane electrodes, typically a smaller surface area is utilized for capacitive gaps compared to radial electrodes. However, this is offset by the fact that planar nature of the electrode structure, which makes it easier to obtain smaller capacitive gaps and helps to compensate for the loss of surface area. In addition, sacrificial layers and wafer-to-wafer bonding techniques can be used to define the capacitive gaps, which makes the process very robust to alignment errors, as the gap uniformity is defined by the thickness of the sacrificial layer and not by the wafer to resonator alignment accuracy. Finally, the metal traces for the electrodes can be defined on the same material used for the resonator (i.e. fused silica), providing uniform coefficient of thermal expansion between the electrode die and the resonator.

Another important parameter to consider is the ratio of out-of-plane motion to in-plane motion, which indicates the transduction efficiency of the out-of-plane electrodes. Finite element modeling using Comsol Multiphysics package revealed that, for mushroom type geometries the ratio of out-of-plane motion to in-plane motion is close to 1:1, leading to very efficient out-of-plane transduction, Fig. 6.

B. Optimization of Q-Factor

Total Q-factor of the vibratory structure can be calculated from contribution of individual dissipation mechanisms in a manner analogous to solving a parallel resistor network, Eq. 1. For this reason the total Q-factor is dominated by the dissipation mechanism with the lowest Q-factor (weakest link).

$$Q_{total}^{-1} = Q_{visc}^{-1} + Q_{anchor}^{-1} + Q_{mat}^{-1} + Q_{surf}^{-1} + Q_{etc}^{-1}. \quad (1)$$

In order to optimize the Q-factor all loss mechanisms affecting the system need to be individually addressed:

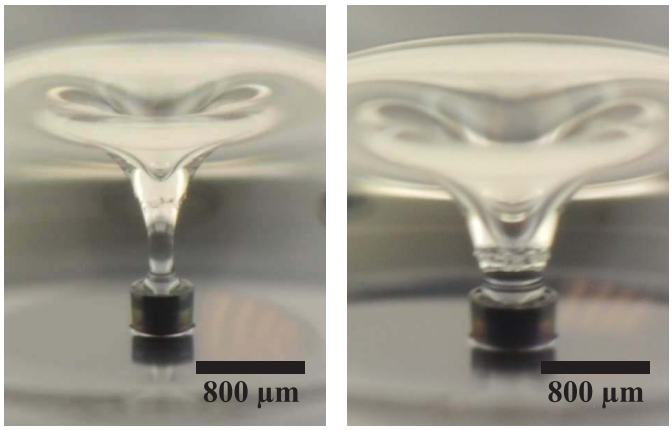

Fig. 7. Small central post diameters create solid stem structures (left), large diameters create hemi-toroidal structures (right).

- Viscous damping, Q_{visc}, is the most dominant affect with Q-factor of several thousands at atmospheric conditions. However, it can easily be eliminated by operating the device in moderate to high vacuum.
- Anchor losses, Q_{anchor}, are caused by acoustic losses into the substrate and are minimized by decoupling the resonator and the substrate through a self-aligned, solid stem structure, Fig. 2.
- Material losses, Q_{mat}, can be divided into several individual loss mechanisms. Thermoelastic dissipation is caused by an interaction between the thermal fluctuations and mechanical oscillations and is minimized by using materials with low coefficient of thermal expansion (CTE), such as fused silica (0.5 ppm/°C). Additional material losses are caused by microscopic effects, such as presence of foreign materials within the matrix of the resonator material and lattice defects at grain boundaries [18]. These effects are minimized by using a high purity, isotropic fused silica material.
- Surface losses, Q_{surf}, are mainly caused by high surface roughness and metallization losses [18]. These effects are minimized through atomically smooth surfaces of micro-glassblown structures [12] and keeping the thickness of the metal layer very small with respect to the resonator shell thickness (50 nm of sputtered Iridium).
- Additional loss mechanisms, Q_{etc}, such as Akheiser dissipation have typically very high Q-factors at kHz range and are not taken into account [19].

III. Modeling

In this section, first analytical expressions to predict the final micro-glassblown geometry will be developed. This will be followed by finite element methods to predict thickness of the shell structure and stem diameter.

In micro-glassblowing, the final device geometry heavily depends on the photolithographic pattern on the wafer surface as well as the etch depth of the cavity. For example, solid self-aligned stem structures were obtained for a central post diameter of 400 μm, whereas hollow hemi-toroidal structures were obtained for a central post diameter of 600 μm, Fig. 7.

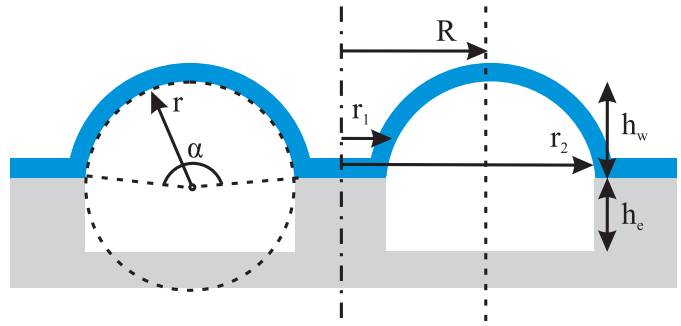

Fig. 8. Geometric parameters of an inverted-wineglass structure: Minor radius r, major radius R, inner perimeter r_1, outer perimeter r_2, etch depth h_e and wineglass height h_w.

For this reason an accurate method to estimate the final geometry from initial dimensions is required.

A. Analytical Solution

In this section analytical expressions for predicting the dimensions of the final inverted-wineglass structure are derived [16]. These expressions can be used to calculate height and minor radius of the structure (h and r) based on the initial cavity dimensions. These expressions assume ideal hemi-toroidal shell structures with zero thickness, as such it is not possible to predict the thickness of the wineglass shell or the diameter of the stem structure.

Calculation starts by finding the volume of the etched cavity:

$$V_{cavity} = \pi(r_2^2 - r_1^2)h_e, \tag{2}$$

where r_2 is the outer perimeter of the cavity, r_1 is the perimeter of the central post, and h_e is the etch depth, Fig. 8. Upon heating, air inside the cavity will expand to fill the volume of the wineglass shell. This volume can be calculated using the ideal gas law:

$$V_{wineglass} = \left(\frac{T_{final}}{T_{initial}} - 1\right)V_{cavity}, \tag{3}$$

where $T_{initial}$ and T_{final} are initial and final glass-blowing temperatures in degree Kelvin. It is assumed that the air inside the cavity is at atmospheric pressure, which is also the pressure of the glassblowing chamber. The volume of the wineglass can also be calculated from geometric parameters using:

$$V_{wineglass} = \pi R r^2(\alpha - \sin(\alpha)), \tag{4}$$

where r is the minor radius, R is the major radius of the partial toroid and α is the fullness parameter in radians (central angle of the arc formed by the minor radius), Fig. 8. Minor and major radii can be removed from the above expression using:

$$r = \frac{r_2 - r_1}{2\sin(\alpha/2)}, \quad R = \frac{r_1 + r_2}{2}. \tag{5}$$

Substituting (2) into (3) and (5) into (4), leaves α to be the only unknown variable, which can be solved numerically. Once α is known, all other parameters of the glassblown shell structure can be extracted using geometric relationships

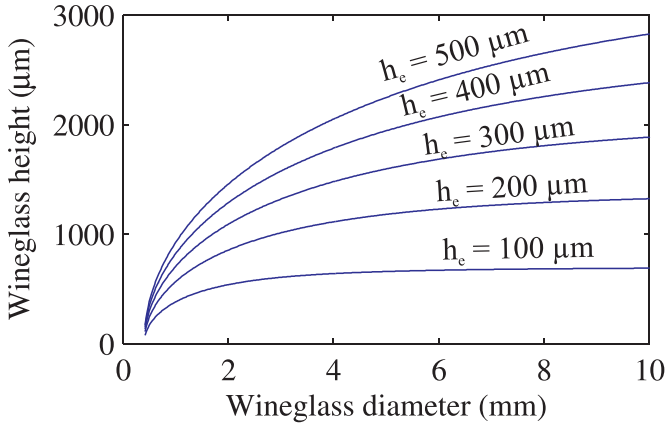

Fig. 9. Analytical solution of etch depth (h_e), wineglass diameter ($2r_2$) vs final inverted wineglass height. Stem outer diameter ($2r_1$) is 400 μm, glassblowing temperature is 875 °C.

in Fig. 8. For example a relationship between minor radius (r), fullness parameter (α) and wineglass height (h_e) can be given as:

$$h_w = r(1 - \cos(\alpha/2)). \tag{6}$$

Solutions of these expressions for a large variety of micro-wineglass structures are presented in Fig. 9. The expressions presented in this section are not sufficient to calculate the shell thickness or the stem diameter, finite element methods to calculate these parameters will be presented in the next section.

B. Finite Element Analysis

As mentioned in the previous section, analytical expressions presented in (2) through (5) are not sufficient to predict the shell thickness and the stem diameter. For this reason, finite element method (FEM) models for micro-glassblowing process were developed to predict the effect of subtle changes in initial dimensions on the final geometry [16].

Due to the large deformation of the shell structure, Arbitrary Lagrangian-Eulerian (ALE) technique [20], [21] was used. ALE allows the mesh to deform, as to track the deformation of the structure in the time domain and reapply the boundary conditions at every time step. Comsol Multiphysics Package was used for the analysis, the following assumptions were used for boundary conditions:

- At the glassblowing temperature (>850 °C for borosilicate glass and >1600 °C for fused silica), the deformation of the glass can be modeled using viscous fluid flow with a viscosity of $10^3 - 10^6$ Pa · s [22].
- The driving force is a slowly varying (quasi-static) uniform pressure field within the shell cavity, Fig. 10.
- Initial pressure inside the cavity is equal to atmospheric pressure.
- Outer surface of the shell is exposed to atmospheric pressure ($P_{gauge} = 0$).
- The surfaces that are bonded to the substrate are not moving (no-slip condition).

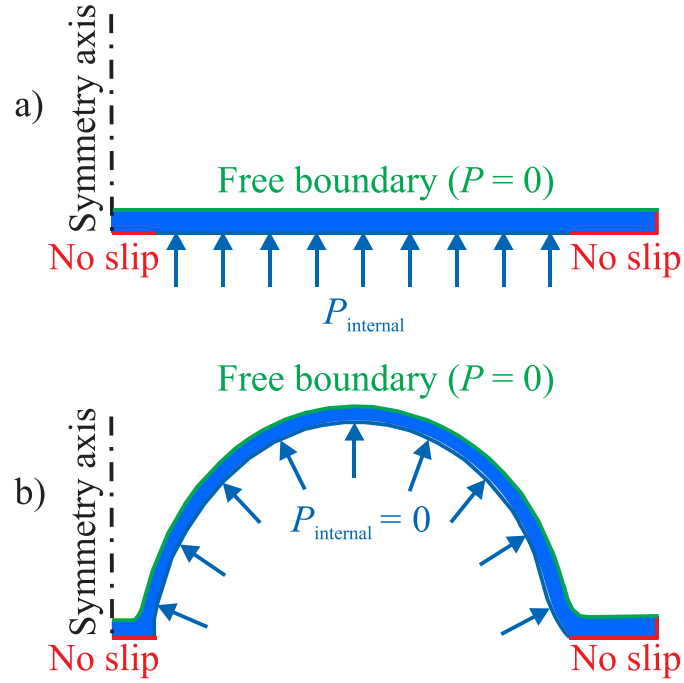

Fig. 10. Boundary conditions for finite element analysis: (a) before glassblowing, (b) after glassblowing.

- The shells are axi-symmetric as such a 2-D axi-symmetric model with <1000 elements is sufficient for solution.

Using the above assumptions, the gauge pressure inside the cavity can be written as:

$$P_{internal} = \frac{T_{final} P_{initial} V_{cavity}}{T_{initial}(V_{cavity} + V_{wineglass})} - P_{initial}, \tag{7}$$

where T is the temperature in degree Kelvin and $P_{internal}$ is applied uniformly to the inner surface of the micro-wineglass structure during glassblowing, Fig. 10.

Since the volume of the wineglass will continuously change during the transient solution, (4) can not be used to calculate $V_{wineglass}$. Instead, a surface integral for the inner surface of the wineglass is used:

$$V_{wineglass} = \oint 2\pi r'^2 dnr, \tag{8}$$

where r' is the distance of any point in the shell structure from the symmetry axis and dnr is the projection of the infinitesimal surface area onto the symmetry axis. (8) allows continuous calculation of the shell volume and consequently the cavity pressure as the structure deforms. This allows the model to reach equilibrium when the final volume is reached ($P_{internal} = 0$).

Fig. 11 shows time domain solution of the micro-glassblowing process and the formation of the self-aligned stem structure. Decreasing the central post diameter from 400 μm to 200 μm is sufficient to change the shell structure from a hemi-toroidal geometry to an inverted-wineglass with a solid stem structure. Fig. 12 shows a side-by-side comparison of the finite element models and the actual fabricated geometries. The results from the models are compared to cross-sectional SEM shots in Table I, showing ~20 % accuracy

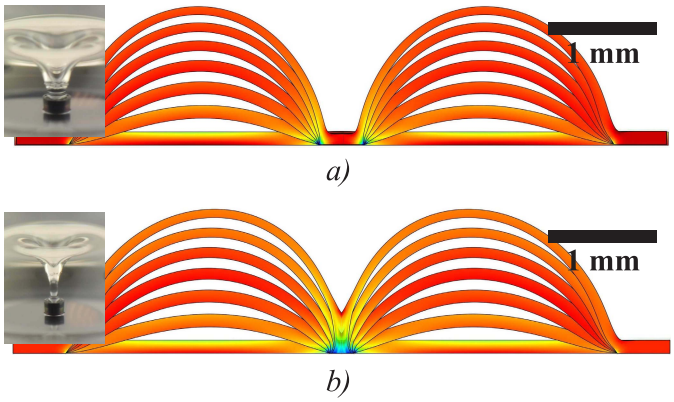

Fig. 11. Transient FEA of micro-glassblowing process showing the formation of self-aligned stem structures. (a) 400 μm stem OD creates a hemi-toroidal structure. (b) 200 μm stem OD creates a hemi-toroidal structure.

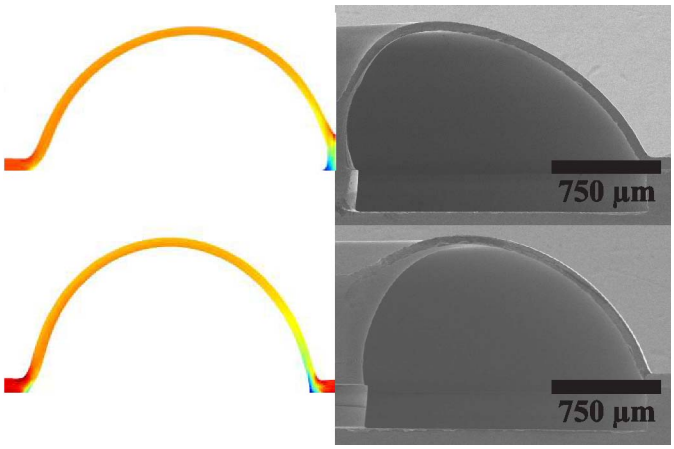

Fig. 12. Finite elemet predictions and cross-sectional SEM shots of fabricated micro-wineglass structures.

TABLE I
COMPARISON OF WINEGLASS DIMENSIONS OBTAINED FROM ANALYTICAL SOLUTIONS, FEA AND EXPERIMENTS

		Device # 1	Device # 2
Initial thickness (μm)		80	300
Outer diameter (mm)		4.2	4.2
Etch depth (μm)		240	200
Glassblowing temperature (°C)		875	1700
Analytical	Final Height (μm)	971	1182
	Thickness (μm)	N/A	N/A
FEA	Final Height (μm)	1025	1260
	Thickness (μm)	52	205
Experimental	Final Height (μm)	832	1288
	Thickness (μm)	44	229

for device #1 and better than 10 % accuracy for device #2 in prediction of final geometry for device. This small variation is attributed to variation in furnace temperature from assumed values.

IV. FABRICATION

Fabrication process utilizes two wafers: a wineglass shell wafer and an electrode wafer. Fabrication process starts with

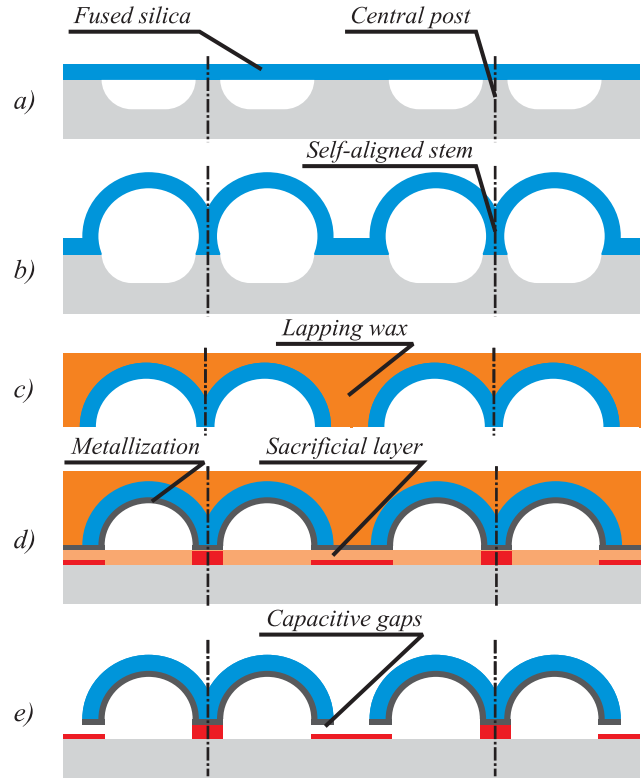

Fig. 13. Wafer-level fabrication process for fused silica micro-wineglass structures. (a) plasma bonding of device layer to substrate with pre-etched cavities, (b) micro-glassblowing at 1700°C, (c) Removal of the substrate via back-lapping, (d) bonding the wineglass wafer to electrode wafer, (e) removal of the sacrifical layer to form capacitive gaps.

LPCVD poly-silicon deposition on 1 mm thick fused silica wafers of up to $\sim 2\mu$m thickness. The poly-silicon mask is later patterned lithographically and is used to etch cavities into fused silica wafers down to $\sim$300 μm in depth. Once the etch is complete, the poly-silicon mask is removed using a 45% KOH bath. The next step of the fabrication process is plasma assisted fusion bonding of a 500 μm thick fused silica device layer (Corning 7980) [12], Fig 13(a). The plasma assisted fusion bonding process for bonding fused silica wafer pairs can be summarized as follows:

1) Cleaning of the wafer pair using solvent and RCA clean,
2) Plasma activation using oxygen plasma (50 Watts power for 2 minutes, 24 sccm O_2 flow),
3) DI water rinse followed by N_2 dry,
4) Contacting of the activated surfaces,
5) Room temperature anneal for >48 hours,
6) Curing the wafer stack at 400 °C for 6 hours.

The bond creates a seamless hermetic seal around the etched cavities without using any intermediate material. The glassblowing is performed at 1700 °C for $\sim$2 minutes and rapidly cooled to room temperature, Fig 13(b). During glass-blowing the device layer at the central post merges to create a solid, self-aligned stem structure, critical for high-Q operation. Shells are released by back-lapping the wafer stack to release using an Allied Multiprep 12" lapping system, Fig 13(c). A series of diamond lapping films with descending grit size of 30 μm $\Rightarrow$ 6 μm $\Rightarrow$ 3 μm $\Rightarrow$ 1 μm $\Rightarrow$ 0.5 μm $\Rightarrow$ 0.1 μm are used for lapping, followed by final polish using 50 nm

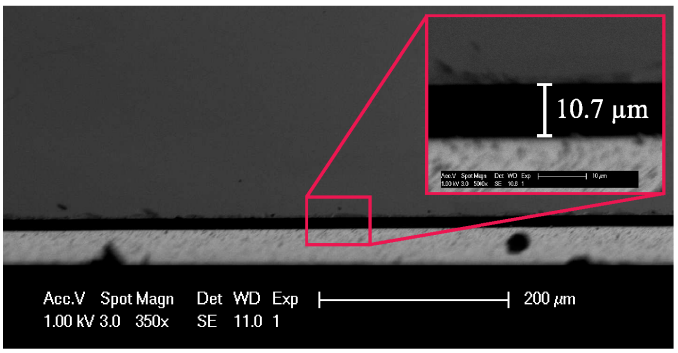

Fig. 14. Uniform 10 μm capacitive gaps have been demonstrated on 7 mm shell structures, resulting in over 9 pF total active capacitance on the device.

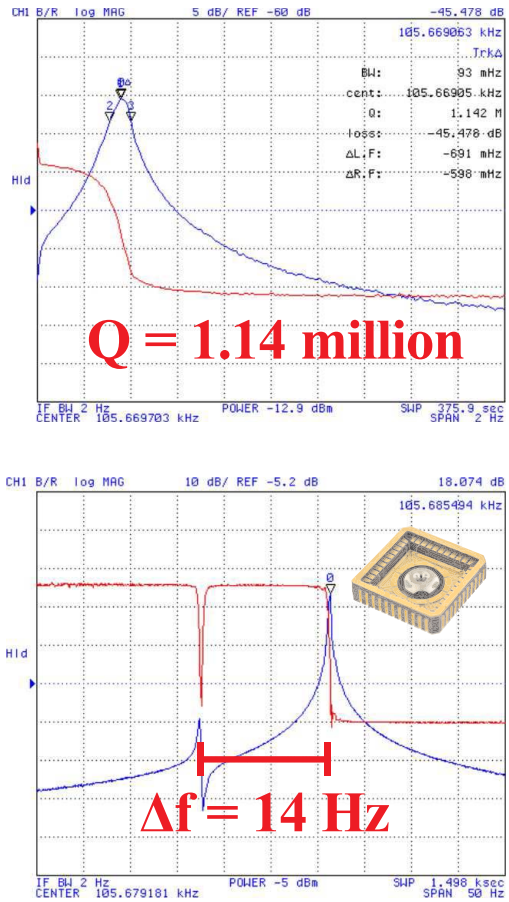

Fig. 15. Frequency sweep revealed a Q-factor of 1.14 million and as fabricated frequency split (Δf) of 14 Hz at 105 kHz center frequency. The chamber pressure was 19 μTorr during the frequency sweep.

colloidal suspension and polishing cloth. Interior surface of the wineglasses is metallized with 50 nm thick sputtered Iridium. Only the interior surface is metallized to minimize the influence of the metal film on the shell resonator. Metallization is performed on a two axis planetary stage for film uniformity, in which the wafer is continuously rotated along z-axis and oscillated $\pm 15°$ along x-axis.

Fused silica out-of-plane electrode structures are fabricated on a separate wafer by blanket coating with Cr/Au (100 nm / 500 nm), spinning a thin layer of photo-resist sacrificial layer and patterning the Cr/Au features using etch-back. In this

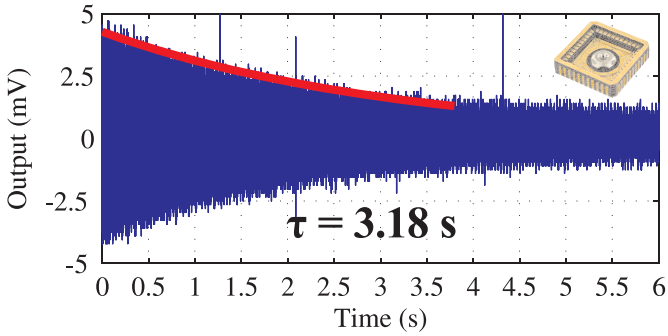

Fig. 16. Ring-down experiment at 19 μTorr shows $\tau = 3.18$ s, giving 1.05 million Q-factor at 105 kHz, confirming the frequency sweep.

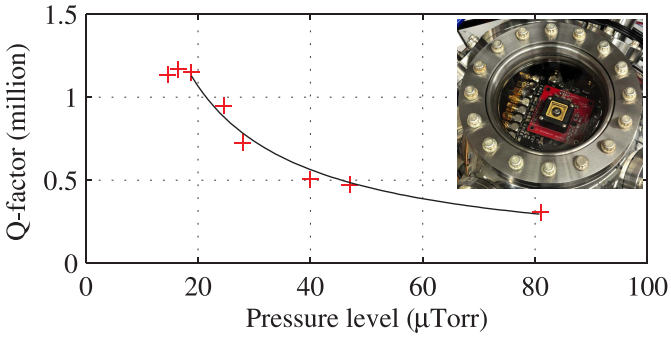

Fig. 17. Q-factor vs pressure level experiment. Q-factors above 1 million were obtained after pumping down to 20 μTorr.

process, the photoresist is used both to pattern the electrodes and as a sacrificial layer to create the capacitive gaps. Subsequently, lapped and metalized wineglass wafer is bonded to the out-of-plane electrode wafer at the stem of each wineglass using low out-gassing epoxy, Ablebond JM7000 or Indium, Fig 13(d). Once the bonding is complete, the sacrificial layer is removed to release the inverted wineglass structures around their perimeter, Fig 13(e), creating capacitive gaps between the metalized inverted wineglass structures and the Cr/Au electrodes, Fig 14.

V. Experimental Results

Frequency sweep using out-of-plane electrodes with $\sim$30 μm capacitive gaps revealed Q-factor of 1.14 million and frequency split of 14 Hz at a center frequency of 105 kHz ($\Delta f/f = 132$ ppm), Fig. 15. Frequency sweep using the same set of forcer and pick-off electrodes showed an amplitude difference of $\sim$30 dB between the two modes, indicative of misalignment between the electrodes and the principle axis of elasticity and/or quadrature coupling between the two modes. A separate ring down experiment was performed where the device was excited with a narrow bandwidth swept sine-wave impulse and resonator output during free vibration was recorded. Ring down experiment demonstrated a time constant of 3.18 seconds and Q-factor of 1.05 million, confirming the frequency sweeps, Fig. 16. In order to observe the effect of viscous damping on the overall Q-factor, the frequency sweep was repeated at different pressure levels. Q-factor of 1 million was obtained below $<$20 μTorr, Fig. 17. No further improvement in Q-factor was observed at 15 μTorr.

TABLE II
SUMMARY OF DEVICE PARAMETERS FOR A 7 mm FUSED SILICA WINEGLASS RESONATOR

Shell diameter	7 mm
Shell thickness	$\sim 500\mu$m
Effective mass	8 μg
Quality factor	$>$ 1 million
Center frequency	105 kHz
Frequency split (Δf)	14 Hz

Subsequently, capacitive gaps as low as 10 μm have been demonstrated on other 7 mm shells, resulting in over 9 pF of total active capacitance within the device (Total dC/dX of 970 nF/m), Fig 14.

VI. CONCLUSIONS

Micro-glassblown fused silica wineglass resonators with out-of-plane electrode structures have been fabricated. Q-factor over 1 million, on both degenerate wineglass modes, and high frequency symmetry ($\Delta f/f$) of 132 ppm have been experimentally demonstrated at a compact size of 7 mm diameter, Table II. In addition, out-of-plane capacitive transduction on MEMS wineglass resonators with 10 μm capacitive gaps have been demonstrated for the first time.

Even though a fairly low frequency split of 14 Hz (132 ppm) was measured, this number is larger than previously reported 0.16 Hz (5.67 ppm) on dry etched borosilicate glass wineglass structures [9]. The increase in frequency split is attributed to the introduction of back-lapping process, which can induce asymmetry in the structure due to edge roughness. High performance degenerate mode gyroscope operation requires an even higher degree of symmetry in order to leverage the high Q-factors seen on 3-D fused silica wineglass resonators. Further improvement in the back-lapping process and addition of post-lapping surface treatment steps might help improve the structural symmetry further.

Low internal dissipation of fused silica combined with high structural symmetry of MEMS micro-glassblowing paradigm may enable batch-fabrication of high performance fused silica wineglass gyroscopes on a wafer surface at a significantly lower cost than their precision-machined macro-scale counterparts.

ACKNOWLEDGMENT

Devices were designed modeled and characterized at UCI Microsystems Laboratory. Fabrication was done at UCI INRF and BION fabrication facilities.

REFERENCES

[1] A. M. Shkel, "Type I and type II micromachined vibratory gyroscopes," in *Proc. IEEE/ION Position, Location, Navigat. Symp. (PLANS)*, 2006, pp. 586–593.

[2] D. M. Rozelle, "The hemispherical resonator gyro: From wineglass to the planets," in *Proc. AAS/AIAA Space Flight Mech. Meeting*, 2009, pp. 1157–1178.

[3] P. Shao, V. Tavassoli, L. Chang-Shun, L. Sorenson, and F. Ayazi, "Electrical characterization of ALD-coated silicon dioxide micro-hemispherical shell resonators," in *Proc. IEEE 27th MEMS*, Jan. 2014, pp. 612–615.

[4] A. Heidari *et al.*, "Micromachined polycrystalline diamond hemispherical shell resonators," in *Proc. TRANSDUCERS EUROSENSORS*, Barcelona, Spain, 2013, pp. 2415–2418.

[5] Y. Xie, H.-C. Hsieh, P. Pai, H. Kim, M. Tabib-Azar, and C. H. Mastrangelo, "Precision curved micro hemispherical resonator shells fabricated by poached-egg micro-molding," in *Proc. IEEE Sensors*, Taipei, Taiwan, Oct. 2012, pp. 279–283.

[6] M. Kanik *et al.*, "Microscale three-dimensional hemispherical shell resonators fabricated from metallic glass," in *Proc. IEEE/ASME Int. Symp. Inertial Sensors Syst.*, Laguna Beach, CA, USA, Feb. 2014, pp. 9–12.

[7] J. Cho, J. K. Woo, J. Yan, R. L. Peterson, and K. Najafi, "A high-Q birdbath resonator gyroscope (BRG)," in *Proc. TRANSDUCERS EUROSENSORS*, Barcelona, Spain, Jun. 2013, pp. 1847–1850.

[8] L. D. Sorenson, X. Gao, and F. Ayazi, "3-D micromachined hemispherical shell resonators with integrated capacitive transducers," in *Proc. IEEE MEMS*, Paris, France, Jan. 2012, pp. 168–171.

[9] D. Senkal, M. J. Ahamed, A. A. Trusov, and A. M. Shkel, "Achieving sub-Hz frequency symmetry in micro-glassblown wineglass resonators," *J. Microelectromech. Syst.*, vol. 23, no. 1, pp. 30–38, 2014.

[10] J. Cho, T. Nagourney, A. Darvishian, B. Shiari, J. Woo, and K. Najafi, "Fused silica micro birdbath shell resonators with 1.2 million Q and 43 second decay time constant," in *Proc. Solid-State Sens., Actuators, Microsyst. Conf. (Hilton Head)*, Hilton Head Island, SC, USA, 2014, pp. 103–104.

[11] D. Senkal, M. J. Ahamed, A. A. Trusov, and A. M. Shkel, "Adaptable test-bed for characterization of micro-wineglass resonators," in *Proc. IEEE 26th MEMS*, Taipei, Taiwan, Jan. 2013, pp. 469–472.

[12] D. Senkal, M. J. Ahamed, A. A. Trusov, and A. M. Shkel, "High temperature micro-glassblowing process demonstrated on fused quartz and ULE TSG," *Sens. Actuators A, Phys.*, vol. 201, pp. 525–531, Dec. 2012.

[13] Y. Okada and Y. Tokumaru, "Precise determination of lattice parameter and thermal expansion coefficient of silicon between 300 and 1500 K," *J. Appl. Phys.*, vol. 56, no. 2, pp. 314–320, 1984.

[14] M. J. Ahamed, D. Senkal, A. A. Trusov, and A. M. Shkel, "Deep NLD plasma etching of fused silica and borosilicate glass," in *Proc. IEEE Sensors*, Baltimore, MD, USA, Nov. 2013, pp. 1767–1770.

[15] E. J. Eklund and A. M. Shkel, "Self-inflated micro-glass blowing," U.S. Patent 8 151 600, Apr. 10, 2012.

[16] D. Senkal, M. J. Ahamed, and A. M. Shkel, "Design and modeling of micro-glassblown inverted-wineglass structures," in *Proc. IEEE/ASME Int. Symp. Inertial Sens. Syst.*, Laguna Beach, CA, USA, Feb. 2014, pp. 13–16.

[17] A. Renault and P. Vandebeuque, "Hemispherical resonator with divided shield electrode," U.S. Patent 6 945 109, Sep. 20, 2005.

[18] B. S. Lunin, "Physical and chemical bases for the development of hemispherical resonators for solid-state gyroscopes," Moscow Aviation Inst., Moscow, Russia, Tech. Rep., 2005.

[19] S. A. Chandorkar, M. Agarwal, R. Melamud, R. N. Candler, K. E. Goodson, and T. W. Kenny, "Limits of quality factor in bulk-mode micromechanical resonators," in *Proc. IEEE MEMS*, Tucson, AZ, USA, Jan. 2008, pp. 74–77.

[20] J. Donea, S. Giuliani, and J. P. Halleux, "An arbitrary Lagrangian–Eulerian finite element method for transient dynamic fluid-structure interactions," *Comput. Methods Appl. Mech. Eng.*, vol. 33, nos. 1–3, pp. 689–723, 1982.

[21] C. W. Hirt, A. A. Amsden, and J. L. Cook, "An arbitrary Lagrangian–Eulerian computing method for all flow speeds," *J. Comput. Phys.*, vol. 253, no. 14, pp. 227–253, 1974.

[22] J. E. Shelby, *Introduction to Glass Science and Technology*. London, U.K.: Royal Society of Chemistry, 2005.

Doruk Senkal received the B.S. degree in mechanical engineering from Middle East Technical University, Ankara, Turkey, in 2007, and the M.S. degree in mechanical engineering from Washington State University, Vancouver, WA, USA, in 2009. He is currently a Graduate Student Research Assistant with the Microsystems Laboratory, University of California at Irvine, Irvine, CA, USA, where he is currently pursuing the Ph.D. degree in mechanical engineering with a focus on microelectromechanical systems (MEMS). His research interests include design and control of degenerate mode gyroscopes, 3-D MEMS wineglass resonators, and microglassblowing of low internal loss materials.

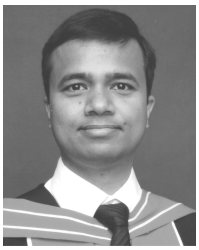

Mohammed J. Ahamed (M'13) is currently a Post-Doctoral Fellow with McGill University, Montreal, QC, Canada, where his research is focused on developing nanotechnology-based next-generation single-cell single-molecule sequencer. He received the B.Sc. and M.Sc. (Hons.) degrees in mechanical engineering from the Bangladesh University of Engineering and Technology (BUET), Dhaka, Bangladesh, in 2002 and 2004, respectively, and the M.A.Sc. and Ph.D. degrees in mechanical engineering from the University of Toronto, Toronto, ON, Canada, in 2006 and 2011, respectively. He was a receipt of the Canadian Commonwealth and Connaught Fellowship. He held a post-doctoral position with the Microsystems Laboratory, University of California at Irvine, Irvine, CA, USA, from 2011 to 2013, where he worked on a DoD-funded project for developing precision rate integrating microgyroscope for aerospace applications. He contributed to teaching as a Lecturer at BUET and as a trainer for teaching assistants at the University of Toronto. He has authored or co-authored dozens of journal and peer-reviewed conference articles. He has served as a reviewer for various journals and conferences. He is a member of the American Society of Mechanical Engineers and the American Physical Society. His major research interest includes design, fabrication, and engineering of micro-electromechanical 3-D inertial sensors, gyroscopes, and micro/nanofluidic-based biomedical lab-on-a-chip.

Mohammad H. Asadian Ardakani received the B.S. and M.S. degrees in mechanical engineering from the Amirkabir University of Technology, Tehran, Iran, in 2007 and 2010, respectively. He is currently pursuing the Ph.D. degree with the Microsystems Laboratory, University of California at Irvine, Irvine, CA, USA. His research interests include design, modeling, and fabrication of 3-D microelectromechanical systems resonators, micromachined inertial sensors, and actuators.

Sina Askari received the B.S. degree in electrical engineering from California State University at Los Angeles, Los Angeles, CA, USA, in 2010, and the M.S. degree in biomedical engineering from the University of Southern California, Los Angeles, in 2012. He is currently pursuing the Ph.D. degree with the Microsystems Laboratory, University of California at Irvine, Irvine, CA. He was with the Department of Sensor Research and Development, Biomedical Industry. His research interests include signal processing, electronic signal conditioning, and development of control algorithm of microelectromechanical systems devices.

Andrei M. Shkel (F'99) received the Diploma (Hons.) degree in mechanics and mathematics from Moscow State University, Moscow, Russia, in 1991, and the Ph.D. degree in mechanical engineering from the University of Wisconsin, Madison, WI, USA, in 1997. In 2000, he joined the faculty of the University of California at Irvine, Irvine, CA, USA, where is currently a Professor with the Department of Mechanical and Aerospace Engineering, with a joint appointment to the Department of Electrical Engineering and Computer Science, and the Department of Biomedical Engineering.

He served as a Program Manager of the Microsystems Technology Office at the Defense Advanced Research Projects Agency (DARPA), Arlington, VA, USA, from 2009 to 2013. His professional interests, reflected in over 200 publications and two books, include solid-state sensors and actuators, micro-electromechanical systems (MEMS)-based neuroprosthetics, sensor-based intelligence, and control theory. He holds 26 U.S. and worldwide patents. His current interests center on the design, manufacturing, and advanced control of MEMS for biomedical and inertial navigation applications, in particular, the development of high-precision micromachined gyroscopes. He has served on a number of Editorial Boards, most recently, as an Editor of the IEEE/ASME JOURNAL OF MICROELECTROMECHANICAL SYSTEMS, an Editorial Board Member of the *International Journal on Smart Structures and Systems*, the Founding Chair of the IEEE International Symposium on Inertial Sensors and Systems, and the General Chair of the 2005 IEEE Sensors Conference. He was a recipient of the IEEE Sensors Council 2009 Technical Achievement Award, the 2005 NSF CAREER Award, the 2002 George E. Brown, Jr. Award, and the 2006 Best Faculty Research Award.

Dr. Shkel received the Office of the Secretary of Defense Medal for Exceptional Public Service for his work at DARPA as a Program Manager in 2013.